

1 **Supplemental Information 1: Methodology**

2 **1.1 Specifications of the Two Resonators and Consistency of  $\Delta\epsilon'$  Values.**

3 This work utilized an open resonator employing microwaves having frequencies between 26.5 and 40 GHz (Resonator No.  
4 1), in contrast to previous work by the authors that used a device emitting frequencies of 15 to 20 GHz (Resonator No. 2)  
5 (Saruya et al., 2022a, b). The use of a different resonator allowed different sizes of ice core samples to be assessed. The  
6 specifications for both resonators and the thicknesses and widths of the samples are summarized in Tables S1 and S2,  
7 respectively. The use of a high frequency band allowed the sample dimensions to be reduced because the beam diameter was  
8 smaller at higher frequencies. The consistency of the data acquired from the present study using Resonator No. 1 with that  
9 from a previous study using Resonator No. 2 was assessed by acquiring  $\Delta\epsilon'$  data across both frequency bands at depths of 2400  
10 to 2500 m. Figure S1 presents a comparison of the dielectric anisotropy profiles and the standard deviations for each 0.5 m  
11 segment, using approximately 23 data points (acquired at 0.02 m intervals) as determined using both resonators. No systematic  
12 differences are apparent in these datasets, although Resonator No. 1 provided a slightly higher standard deviation based on the  
13 smaller beam diameter of this instrument. The grain numbers included in the Gaussian beams or thin sections are provided in  
14 Table S3. The quantity of crystal grains in the beam or thin section affected the statistical significance level for the data and,  
15 in some cases, a moving average of data acquired along the core was used to increase the significance level.

16 Table S1: Specifications for the two resonators

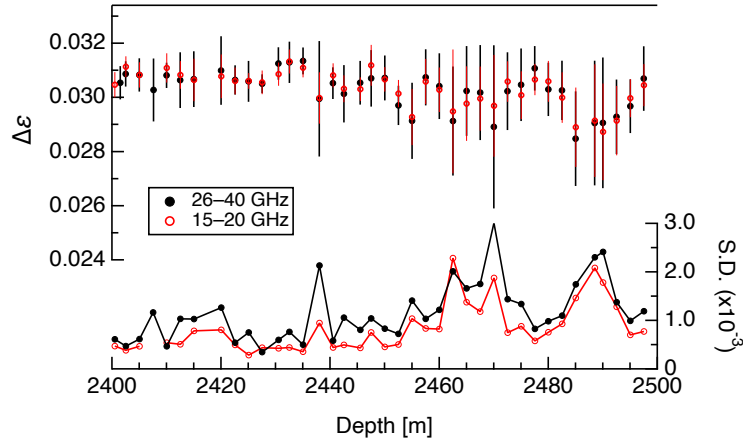
Item	Curvature radius of the concave mirror (mm)	Distance between two mirrors (mm)	Scale diameter of the beam on the flat mirror (mm)	Frequencies (GHz)	Depths range (m)
Symbol	$R$	$D$	$\omega$	$F$	$z$
Resonator No.1	120	110	16	26.5– 40	2400–2970
Resonator No.2	250	225	38	14–20	100–2500

17 Table S2: Thicknesses and widths of the samples

Depths range (m)	Thickness (mm)	Width (mm)	Resonators used
2400–2500	35–37	53–58	No.1 and No.2
2500–2970	41–42	30–38	No.1

18 Table S3: Grain numbers included in the Gaussian beams or thin sections

Grain area	Dimensions (mm)	0.1 cm <sup>2</sup>	0.3 cm <sup>2</sup>	0.5 cm <sup>2</sup>	1 cm <sup>2</sup>	2 mm <sup>2</sup>	4 cm <sup>2</sup>
Thick-section-based method							
DTM No.1	~ø16 × ~40	353	68	32	11	4	1
DTM No.2	~ø38 × ~70	3490	672	312	110	39	14
Thin-section-based methods							
Laue X-ray diffraction method	100 × 45	450	150	90	45	23	12
Microscopy and G50	90 × 50						



20

21 **Figure S1.** Comparison of the  $\Delta\epsilon'$  values and associated standard deviations obtained using Resonators No. 1 (black) and No. 2 (red).

22

## 1.2 Inclination of the $c$ -axes cluster and the DTM

23

24

25

26

27

28

29

30

31

32

33

34

35

36

37

38

39

40

41

42

43

44

45

46

47

48

49

Figure 2 in the main text shows the sample geometries and the open resonator setup. In the case that the  $c$ -axes cluster aligns with the vertical direction (i.e., the ice core axis), it is relatively straightforward to obtain an angle of approximately  $45^\circ$  between this cluster and the electric field. This was the case for ice obtained from depths of less than approximately 2400 m (Saruya et al., 2022b). Figure S2 presents an example of this frame projected onto a Schmidt net. In this frame, the axis of the  $c$ -axes cluster is always orthogonal to the incident beam and so is situated on the plane of the electric field vector. However, issues arise when the  $c$ -axes cluster deviates from the vertical. Depending on the inclination angle of the  $c$ -axes cluster relative to the zenith and the rotation of the cylindrical ice core in the horizontal direction, the axis of the  $c$ -axes cluster may not align with the plane of the electric field vector (Figure S2b). In such cases, the DTM determines the permittivity components projected onto the plane of this vector, which correspond to the non-principal components of the tensorial permittivity. Consequently, the raw values of the non-principal components of the dielectric anisotropy,  $\Delta\epsilon'$  (as shown in Figure S2b), will be smaller than the principal components of  $\Delta\epsilon$  if the  $c$ -axes cluster axis aligns with the plane of the electric field vector. The  $\Delta\epsilon'$  values can be corrected to  $\Delta\epsilon$  data only if both the angle of inclination and the horizontal orientation of the  $c$ -axes cluster are known (see Figure S2b').

It is helpful to examine Figure S2 in greater detail to better explain the measurement principles used in this research. Figure S2a depicts the scenario in which the  $c$ -axes cluster of the single pole fabric aligns with the vertical direction. The diagram's centre represents the incident axis of the microwave beam in the resonator and the electric field vector is always orthogonal to the beam, spreading along the diagram's periphery. The dark blue plane contains the girdle of the  $a$ -axes while the red line indicates a plane that includes both the beam axis and the  $c$ -axes cluster. In this setup, setting the electric field vector to approximately within the direction of  $\mathbf{E}_1$  or  $\mathbf{E}_2$  splits the vector components into two directions. This allows derivation of the two permittivity components  $\epsilon_v$  and  $\epsilon_h$  as permittivities in the two principal axes along the diagram's periphery. Figure S2b illustrates a scenario in which the  $c$ -axes cluster for the single maximum fabric is inclined in an arbitrary horizontal direction. The diagram's centre is again the incident axis of the microwave beam. The dark blue plane contains the girdle of the  $a$ -axes whereas the red line indicates a plane containing both the beam axis and the  $c$ -axes cluster. The dashed line indicates a plane perpendicular to the red plane and containing the beam axis. In this arrangement, setting the electric field vector to approximately within the rotated direction of  $\mathbf{E}_1$  or  $\mathbf{E}_2$  still splits the vector components into two directions. However, this scenario results in two non-principal components,  $\epsilon'_v$  and  $\epsilon'_h$ , as the permittivity. Knowing the angle of inclination of the  $c$ -axes cluster ( $\theta$  in Figure S2b') and the horizontal orientation of the  $c$ -axes cluster allows  $\Delta\epsilon$  values to be determined accurately

by rotating around the core axis to align the  $c$ -axis maximum within the plane of the electric field vector (as shown in Figure S2b') and by calculating the geometrical effects of the angle of inclination of the  $c$ -axes cluster.

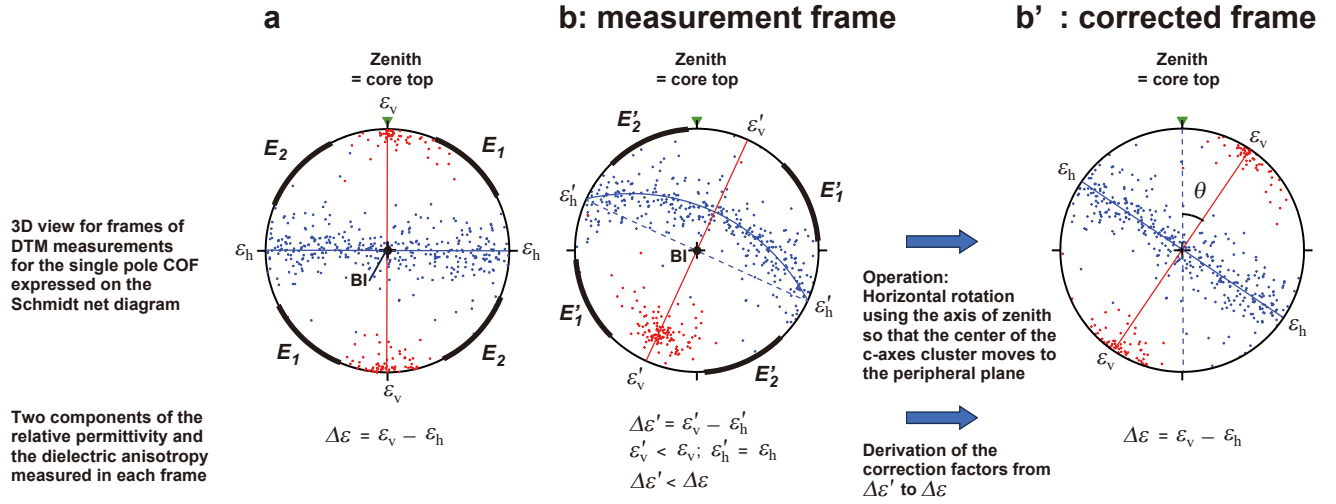


**Figure S2.** An explanation of the three-dimensional geometry of systems composed of core samples, crystal axes and applied electric fields, represented using projections on Schmidt net diagrams. In all figures, both the  $c$ -axes (red dots) and  $a$ -axes (dark blue dots) are presented for an imaginary ice core sample. In (a) and (b), the centre of the diagram represents the axis of incidence of the microwave beam, with the peripheral circle forming a plane orthogonal to the beam. The top of this peripheral circle corresponds to the vertical orientation within the ice sheet, which is also the top of each ice core. (a) The  $c$ -axes cluster of the single pole fabric aligns with the vertical direction and the  $a$ -axes girdle lies on the horizontal plane. In the case that the electric field vector of the microwave beam falls within the orientation range of  $E_1$  or  $E_2$ , birefringence is induced that allows the two permittivity components  $\epsilon_v$  and  $\epsilon_h$  to be determined as the principal components of the tensor. Consequently, the difference  $\Delta\epsilon$  can be calculated. (b) The plane perpendicular to the  $c$ -axes cluster of the single pole fabric is inclined in an arbitrary horizontal orientation while the girdle of the  $a$ -axes deviates from the beam axis. In this scenario, using the electric field vectors from (a) within the orientation range of  $E_1$  or  $E_2$  does not produce birefringence because the splitting of the waves into two components is not equally balanced. However, if the microwave beam's electric field vector is within the inclined range from  $E_1$  or  $E_2$ , meaning  $E'_1$  or  $E'_2$ , balanced birefringence is achieved and it becomes possible to derive two non-principal components of permittivity,  $\epsilon'_v$  and  $\epsilon'_h$ . This permits calculation of the non-principal difference as  $\Delta\epsilon'$ . (b'): The identical scenario to (b) except that the system has been rotated horizontally so that the  $c$ -axes cluster aligns with the periphery of the diagram where the electric field vector is located. By comparing permittivity values for cases (b) and (b') based on the  $c$ -axis fabric data, the factors required to adjust  $\Delta\epsilon'$  values to  $\Delta\epsilon$  values can be obtained.

### 1.3 Details of the layer inclination analyses

The inclinations of the layers in the DF ice core were determined using two methods. The core specimens contained faint, thin, cloudy bands with thicknesses ranging from approximately 1 to 10 mm. These core samples were observed using a light stage, approximately 250 by 600 mm in size, placed on a table. These samples each represented a half vertical cut of the original cylindrical form and were visually inspected by looked directly down at the core from above the light stage, with the sample positioned between the observer's eyes and the light stage. The cloudy bands could only be seen when oriented vertically and appeared as sharp lines. At other angles it was difficult to recognize the layers. By orienting the layers vertically and maintaining an orthogonal relationship to the core's inclination on the light stage, the angle of inclination of each ice core sample could be determined using a large protractor. Based on this procedure, layer inclinations were ascertained three-dimensionally by assessing the maximum angle of inclination. In the second method, the observer used the coordinates of three or more points in each layer within the ice core samples representing half of the original core. Using these points, the angle of inclination of the layer was determined in three dimensions, ensuring the orientation was at the point of maximum layer inclination. At least two observers (in most cases, Miyamoto and Fujita) measured the angle for each layer as a cross-check. Additionally, measurements were repeated several times to improve technique and confirm reproducibility. The observers estimated that the maximum error in this process was on the order of 5°. The orientation of the inclination was not

83 recorded because core orientation was not of interest at that time, although observers did assess whether the horizontal  
 84 orientation of the *c*-axes cluster and the normal axis of the layer inclination were within the same vertical plane. This was  
 85 found to be the case throughout the LO20%.

#### 86 **1.4 Estimation of the error range of the normalized eigenvalues for the *c*-axis fabric data obtained through thin-** 87 **section methods**

88 In general, for *N* grain samples (with *N* ranging from approximately 50 to 250 for the Laue X-ray analyses in the present  
 89 work), the addition of a grain will cause the normalized eigenvalue to vary by approximately 1/*N* at most. However, if the *c*-  
 90 axes are clustered, as in the DF core, this variation will be much smaller. Specifically, assuming each grain contributes an  
 91 eigenvalue between 2/3 and 1 (see Figure 5a), the range of variation will be 1/(3*N*) or less. Therefore, the total number of  
 92 grains is a very important factor and the error in the eigenvalues in this study is on the order of 1/(3*N*) or less.

#### 93 **1.5 Microstructural observations**

94 Grain shapes were assessed using the ImageJ software package and Table S4 summarizes the resulting mean aspect ratios,  
 95 defined as the ratio of the long axis of a fitted ellipse to the short axis. This table also provides sample depths, concentration  
 96 of dust particles and standard deviations of the aspect ratios. For certain depths, several thin sections were used to obtain a  
 97 sufficient number of crystal grains for analysis (as noted in the table). Grains that were flattened (or elongated in two  
 98 dimensions) were identified in samples from depths of 2540, 2648, 2653.5, 2673.5 and 2759.5 m (as indicated by the brown  
 99 shading in Figure 5) and had aspect ratios ranging from 1.9 to 2.0. In contrast, the aspect ratios in the deep impurity-rich layers  
 100 (in samples from depths of 2907.5 and 2949 m) and in impurity-poor layers ranged from 1.5 to 1.6. The specimens from depths  
 101 of 2518.5 and 2540 m were located in impurity-rich layer (see Figure 5). The concentration of dust particles in the 2518.5 m  
 102 specimens was not as high (~32 ppbv) and there was no evident elongation while the aspect ratio was smaller.

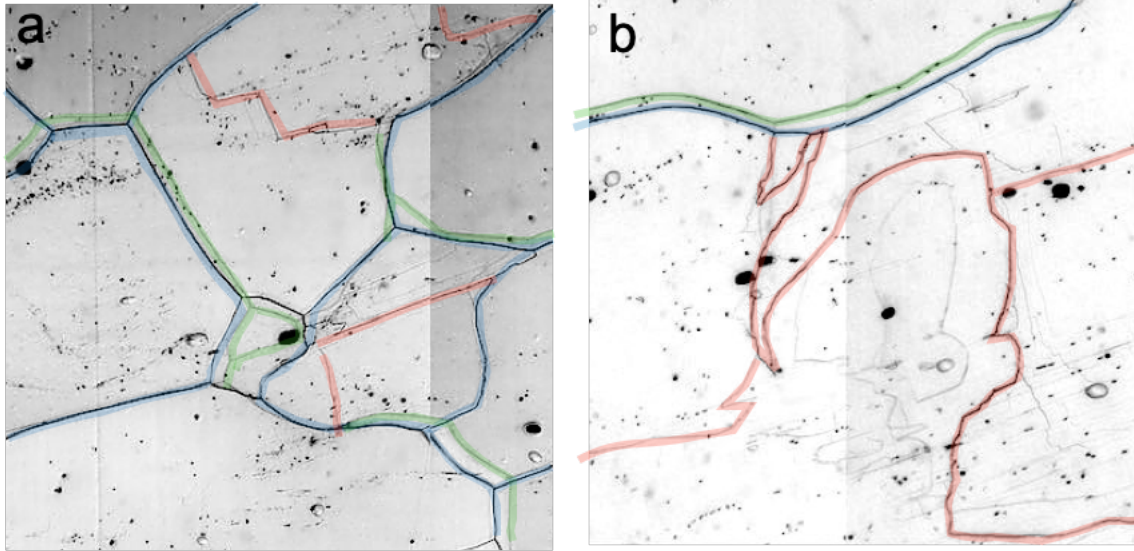
103 Table S4: Aspect ratios of grains in thin sections as determined using the Image J software package. Sample depths,  
 104 concentrations of dust particles, grain numbers, means and standard deviations (SDs) are provided. The columns with bold  
 105 text provided data for samples from an impurity-rich layer having slanting and flattened (or elongated in two dimensions)  
 106 grains.

Depth [m]	2470	2490	2500	2518.5	<b>2540</b>	2623.5	<b>2648</b>	<b>2653.5</b>	<b>2673.5</b>
Concentration of dust particles [ppbv]	~3	~1	~7	~32	<b>~132</b>	~4	<b>~273</b>	<b>~221</b>	<b>~166</b>
Grain number	122 <sup>a)</sup>	90 <sup>b)</sup>	44	121	<b>167</b>	43	<b>335</b>	<b>238</b>	<b>244</b>
Average aspect ratio	1.7	1.6	1.7	1.7	<b>1.9</b>	1.5	<b>2.0</b>	<b>1.9</b>	<b>1.9</b>
SD	0.6	0.5	0.5	0.6	<b>0.5</b>	0.3	<b>0.7</b>	<b>0.6</b>	<b>0.6</b>

2685	2730	<b>2759.5</b>	2807	2847.5	2868	2872	2887	2907.5	2949
~12	~10	<b>~137</b>	~4	~34	~2	~3	~10	~91	~51
55	96	<b>262</b>	44	107 <sup>a)</sup>	41	42 <sup>a)</sup>	45	56	48
1.6	1.6	<b>1.9</b>	1.5	1.5	1.6	1.6	1.5	1.6	1.5

- 108 a) Sum of two thin sections.  
 109 b) Sum of three thin sections.

110 Figure S3(a and b) show enlarged images of microstructures. Each panel corresponds to the upper right sections of the  
 111 images in Figures 7a and b. Grain boundaries, grain boundaries on the reverse side and subgrain boundaries identified based  
 112 on geometry are all indicated by shading.



113  
 114 **Figure S3.** Enlarged images showing the microstructures of samples from depths of 2648 (left) and 2685 m (right). Each figure  
 115 corresponds to the upper right of the original image in Figures A1a and A2b in Appendix A. Grain boundaries (blue lines),  
 116 grain boundaries on the reverse side (green lines) and subgrain boundaries (red lines) determined based on geometry are shown.  
 117 Scale bar: 2 mm.

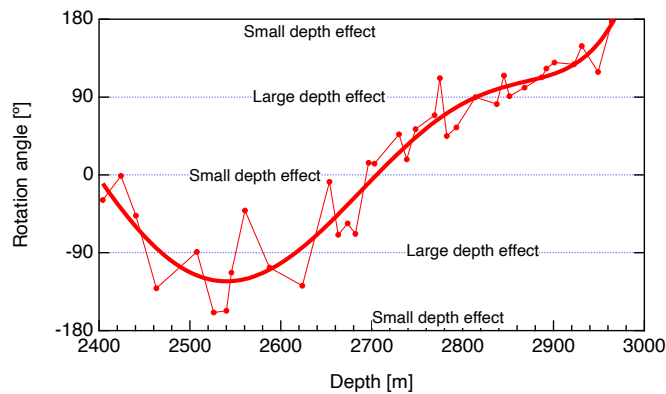
118  
 119

120 **Supplementary Information 2: Corrections from  $\Delta\epsilon'$  to  $\Delta\epsilon$**

121 Using data from the Laue X-ray diffraction measurements taken at 42 different depths, both the angles of inclination and  
122 the horizontal orientations of the *c*-axes clusters were assessed. It was assumed that the angle of inclination of the *c*-axes  
123 cluster consistently moved towards the same horizontal orientation within the ice sheet. This was considered a valid  
124 assumption given the low probability of horizontal rotation in an ice flow under deep englacial conditions at the dome summit.  
125 It should be noted that this angle may rotate with increasing depths if the dome summit position migrates in a complex manner.  
126 Another possibility is that the continuity of orientation between adjacent cores may be lost when handling a large number of  
127 such specimens, especially when irregular ice core breaks occur. During DTM analyses, the core orientation was not known  
128 in advance and the orientation could only be obtained from the Laue data or from the layer inclination values if such values  
129 were recorded. These assumptions were required to correct  $\Delta\epsilon'$  values to obtain  $\Delta\epsilon$  data. The results for angles of inclination  
130 of the *c*-axes clusters are presented in Figure 5f of the main text and demonstrate that the horizontal orientation of the *c*-axes  
131 cluster gradually rotated with increasing depth (Figure S4). As shown in this figure, curve fitting was used to address the  
132 degree of data scatter. Notably, such scatter between approximately 2400 and 2700 m produced significant deviations from  
133 the fitted curve. The tensorial components of *c*-axes projected onto the diagram's periphery were calculated and eigenvalue  
134 anisotropy (the difference between the maximum and minimum) were computed by combining the angle of inclination of the  
135 *c*-axes cluster (Figure 5f) and the horizontal orientation of the *c*-axes cluster (Figure S4). This process was performed for  
136 orientations for which the *c*-axes cluster aligned with the periphery of the Schmidt net diagram (as shown in Figure S2b').  
137 The results are presented in Figure S4. Using these data, the coefficients necessary to obtain  $\Delta\epsilon$  from  $\Delta\epsilon'$  were estimated, as  
138 detailed in Figure S5. The necessary corrections were found to be minor (at most several percent) at depths shallower than  
139 approximately 2730 m but became more significant (up to approximately 20 percent) at greater depths. Between  
140 approximately 2400 and 2730 m, over which range large deviations from the fitting curve were observed (Figure S4), the  
141 resulting errors in the corrections were likely limited because the angle of inclination of the *c*-axes cluster remained small  
142 (less than about 20°) throughout this depth range (Figure 5c). Therefore, the errors in the present correction coefficients are  
143 estimated to be less than 10%.

144 Figure S7 displays the  $\Delta\epsilon'$  and  $\Delta\epsilon$  values along with eigenvalue anisotropy data obtained from the Laue X-ray diffraction  
145 measurements. At depths exceeding 2900 m, the corrections incorporate errors because of continuity uncertainties between  
146 core samples arising from unpredictable core rotation. Consequently, the apparent sudden changes in  $\Delta\epsilon$  values may be  
147 erroneous. Nevertheless, there is good agreement between the  $\Delta\epsilon$  values from the DF and EDC ice cores at ages older than  
148 approximately 630 kyr BP, corresponding to the ice age at 2900 m.

149



150

151 **Figure S4.** Horizontal orientation of the *c*-axes cluster (left axis) as derived from the *c*-axis fabric data obtained via Laue X-ray diffraction  
152 measurements. Angles of 0°, 180° or -180° indicate that the *c*-axes cluster was perpendicular to the observer's line of sight and parallel to  
153 the electric field vector of the electromagnetic waves. Conversely, angles of 90° or -90° indicate that the *c*-axes cluster was parallel to the

observer's line of sight and perpendicular to the electric field vector. In the case of horizontal orientation of the  $c$ -axes cluster with an angle of  $0^\circ$ ,  $180^\circ$  or  $-180^\circ$ , the cluster was aligned with the periphery of the Schmidt equal area projection.

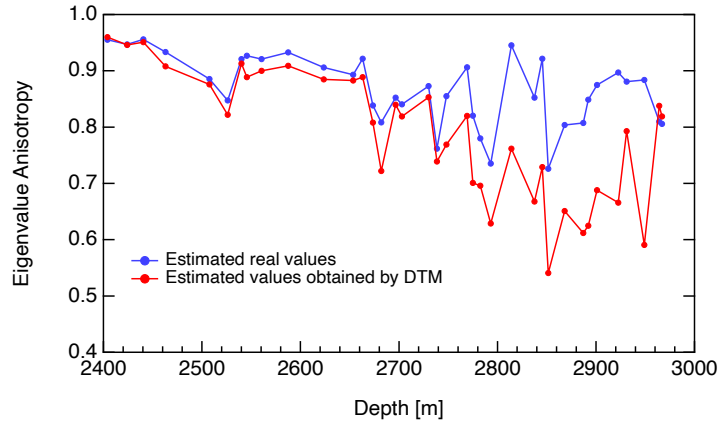


**Figure S5.** Comparison of eigenvalue anisotropy values associated with the measurement frame (indicated in red) and the corrected frame (indicated in blue).

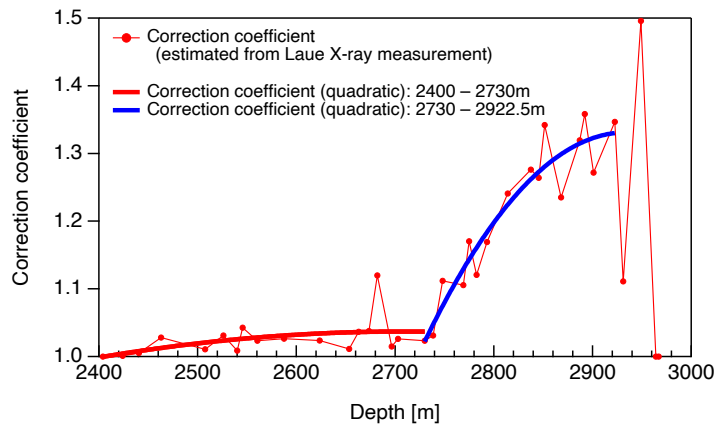


**Figure S6.** Correction coefficients for the conversion of  $\Delta\epsilon'$  values to  $\Delta\epsilon$  data. Proposed fitting curves for depths ranging from 2400 to 2730 m and for depths greater than 2730 m are shown.

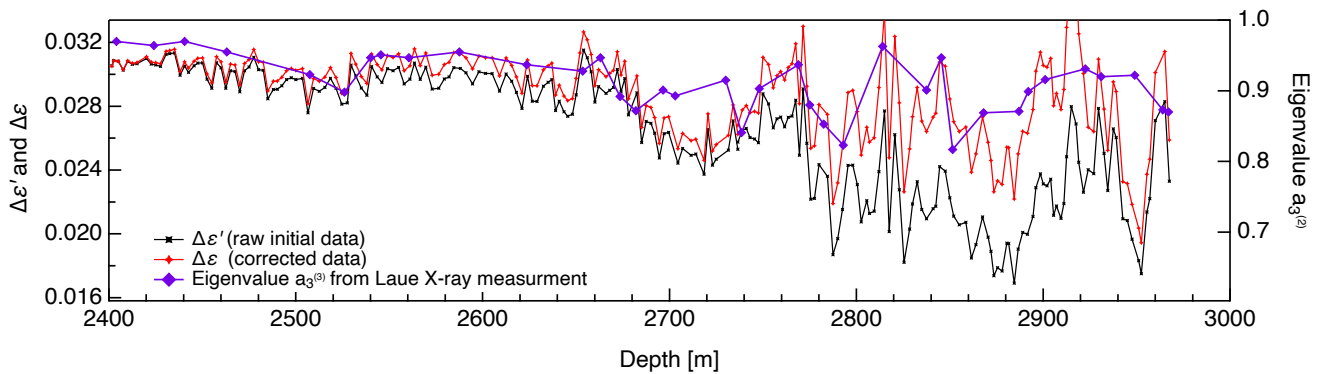


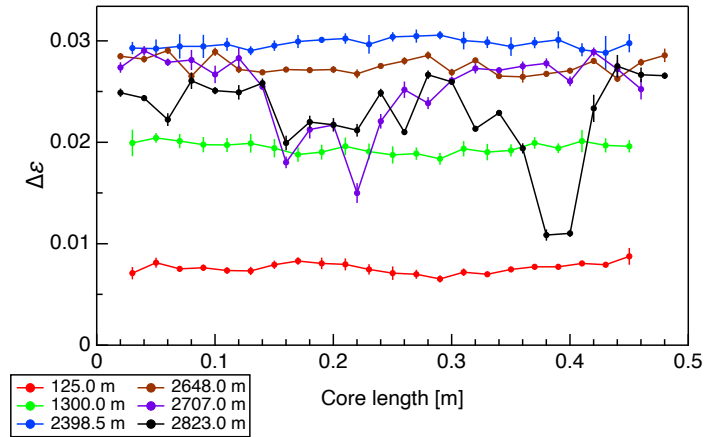
**Figure S7.** Correction of  $\Delta\epsilon'$  (depicted in black) to  $\Delta\epsilon$  (red) and comparison with eigenvalues,  $a_3^{(2)}$  (purple), estimated from Laue X-ray diffraction measurements. It is important to note that the DTM data represent mean values for each 0.5 m section and were acquired using thick sections whereas the Laue X-ray diffraction data were derived from thin sections. The volume of ice represented by a single data point differed between these two techniques by a factor of approximately  $10^2$ . The DTM approach also provided volume-weighted values for the  $c$ -axis fabric whereas the Laue X-ray diffraction measurements gave a mean value across the total number of crystal grains, typically not accounting for the size (or volume) of each individual crystal grain.





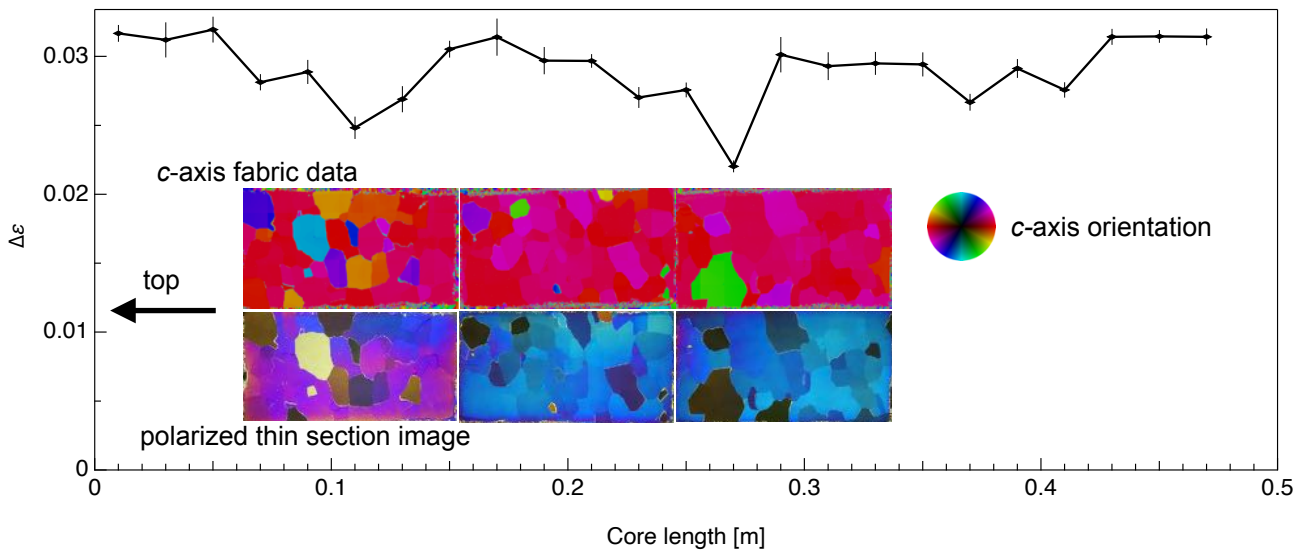
173 **Supplementary Information 3: Continuous Variations in  $\Delta\epsilon$  and Comparison with Microstructures**

174 Figure S8 presents examples of the continuous variation of  $\Delta\epsilon$  across 0.5 m core samples at five depths (125.0–125.5,  
175 1300.0–1300.5, 2648.0–2648.5, 2707.0–2707.5 and 2823.0–2823.5 m). The data for the shallowest two depths were obtained  
176 from Saruya et al. (2022b). The mean values and SDs for each 0.02 m segment were calculated using various TEM  $_{0,0,q}$   
177 resonance modes in conjunction with the open resonator method. The mean values (SD) over these five depth ranges were  
178 determined to be 0.0076 (0.0005), 0.0194 (0.0006), 0.0285 (0.0008), 0.0263 (0.0036) and 0.0282 (0.0043), respectively.  
179 Fluctuations within the 0.5 m ice core samples become more pronounced at greater depths. However, in the case of the core  
180 sample having a higher concentration of dust particles (at 2648.0 m, represented by brown points), the fluctuations are not as  
181 marked.  
182



183 **Figure S8.** Examples of variations in  $\Delta\epsilon$  along 0.5 m sections of ice cores as determined by continuous measurements. The bars indicate  
184 standard deviations associated with various resonance modes in the open resonator.  
185

186  
187 Figure S9 presents an example of a comparison of the  $\Delta\epsilon$  profile with microstructures for the depth range of 2490.0–2490.5  
188 m. The upper and lower panels show fabric data and polarized images, respectively. Within the  $\Delta\epsilon$  profile, two locations exhibit  
189 lower  $\Delta\epsilon$  values (at 0.11 and 0.27 m). At these depths, grains were observed having  $c$ -axis orientations differing from those of  
190 the surrounding grains. These layers contributed to a decrease in the mean  $\Delta\epsilon'$  value and an increase in the SD for this 0.5 m  
191 core section.  
192



194 **Figure S9.** An example of a comparison of variation in  $\Delta\epsilon$  along a 0.5 m ice core section with microstructures based on *c*-axis fabric data  
195 and polarized images obtained from thin sections over the depth range of 2490.0–2490.5 m. The bars in the  $\Delta\epsilon$  variation graph indicate  
196 standard deviations associated with different resonance modes of the open resonator. The horizontal scales in both the  $\Delta\epsilon$  variation graph  
197 and the microstructural images are aligned for consistency.  
198  
199